

Focused fields of ultrashort radially-polarized laser pulses having low-order spatio-temporal couplings

Spencer W. Jolly^{1,2,*}

¹*LIDYL, CEA, CNRS, Université Paris-Saclay, CEA Saclay, 91191 Gif-sur-Yvette, France*

²*Brussels Photonics Team (B-PHOT), Dept. of Applied Physics and Photonics, Vrije Universiteit Brussel, Pleinlaan 2, 1050 Brussels, Belgium*

(Dated: October 22, 2021)

We present a detailed study of the fields and propagation characteristics around the focus of ultrashort radially-polarized laser beams (RPLBs) having low-order spatio-temporal couplings (STCs). The three STCs considered are the focusing of the different frequencies to different positions along the longitudinal coordinate, the focusing of the frequencies to different positions along one transverse coordinate, and the beam waist or Rayleigh range having a dependence on frequency. The STCs considered are deemed low-order because they are primarily linear in frequency. The combination of a low-order vector beam, ultrashort pulse duration, and the three different STCs shows promise for exotic applications in dielectric or charged particle manipulation and potentially other strong-field phenomena. The STCs presented are all developed in a standard frequency-domain model where each case involves a different chromatic term. We present the results unique to the vector nature of the RPLBs and compare them to the linearly polarized cases, opening up opportunities for control of the electric field around the focus with the additional element of polarization.

I. INTRODUCTION

Radially-polarized laser beams (RPLBs), a unique solution to Maxwell's equations with primarily radial polarization, are a low-order vector beam (having spatially-varying polarization) that can have a very tight focus [1, 2] and have applications in microscopy [3–5] and manipulation of micro-particles [6–9] for example. Ultrashort RPLBs require additional modeling due to their broad bandwidth and can be applied to particle acceleration [10–15] and potentially high-harmonic generation and other realms of high-field nano-optics [16]. Combing these ultrashort RPLBs with spatio-temporal couplings (STCs)—aberrations that lead to unseparable space-time or space-frequency electric fields [17]—results in interesting properties. In this manuscript we present frequency-domain models to describe RPLBs having different STCs and investigate potentially valuable phenomena unique to the vector nature of RPLBs.

We first describe the standard ultrashort RPLB in frequency space, and describe its basic properties. Then we compare certain properties of the RPLB when it has three different low-order STCs (i.e. generally linear in frequency dependence). The three STCs considered are: the focusing of the different frequencies to different positions along the longitudinal coordinate, longitudinal chromatism; the focusing of the frequencies to different positions along one transverse coordinate, spatial chirp; and the beam waist or Rayleigh range having a power-law frequency dependence; referred to as frequency-dependent beam parameters.

In the case of each STC there are general effects around the focus, which often involve an increase in the inte-

grated beam size or an increase in the pulse duration (and equivalently a decrease in the intensity), similar to with linearly-polarized pulses [18]. But in addition to those general effects there are more nuanced effects in each case, which can involve the pulse temporal profile, spatial intensity profile, or its behavior during propagation away from the focus. In the case of longitudinal chromatism there is an effective increase in the Rayleigh range due to the longitudinal separation of the frequencies, and an additional effect when combined with temporal chirp where the velocity of the intensity peak can be different than the speed of light c , called the flying focus. For spatial chirp there can be wavefront rotation, where the wavefront in focus points in different directions over time, and there can also be a tilt in the arrival time of the pulse when combined with temporal chirp. In the case of the frequency-varying beam parameters we consider the evolution of the carrier-envelope offset phase, which differs from the Gouy phase in a non-trivial fashion.

Indeed all of the above phenomena have been described and measured experimentally for linearly-polarized ultrashort laser pulses. In the case of the RPLBs which we describe theoretically here, there is first the fact that the model for the fields is different, resulting in different precise descriptions for each phenomenon. But there is also the crucial fact that RPLBs are vector beams and the different polarization components of the electric field not only have different basic properties that influence how to look at the effect of STCs on each polarization, but the different components are also described via different equations resulting in different behavior. In each case we develop the model for the RPLB with STCs using the same frequency-space model as for the standard ultrashort RPLB, but clearly explain the modified or added terms which result in the fundamental changes in beam properties or propagation effects. Because the STCs add non-trivial space-frequency terms in our model we do not

* spencer.jolly@vub.be

have the ability to solve for the fields in time, but can present results in time based on our model using numerical Fourier-transforms.

II. STANDARD ULTRASHORT RPLB

In the following model we use pulses that have Gaussian spatial and spectral/temporal profiles, with characteristic widths s_0 and τ_0 respectively, at a central wavelength λ_0 ($\omega_0 = 2\pi c/\lambda_0$) and the Rayleigh range $z_R = \omega_0 s_0^2/2c$. The fields of the focused ultrashort RPLBs are modeled in the frequency domain as in Refs. [19–21] using the proper form for the longitudinal fields including only paraxial terms. With $A_\omega = \exp(-\delta\omega^2/\Delta\omega^2)$, $\Delta\omega = 2/\tau_0$, and $\delta\omega = (\omega - \omega_0)$ we have the solutions for the radial electric field E_r , longitudinal electric field E_z , and azimuthal magnetic field B_θ

$$\tilde{E}_r(\omega) = A\epsilon\rho C_2 \quad (1)$$

$$\tilde{E}_z(\omega) = A\epsilon^2 [S_2 - \rho^2 S_3] \quad (2)$$

$$\tilde{B}_\theta(\omega) = \frac{\tilde{E}_r(\omega)}{c}, \quad (3)$$

where the tilde denotes frequency space, $\rho = r/s_0$ and $\epsilon = s_0/z_R$, and

$$A = \frac{\omega_0}{2c} \sqrt{\frac{8P_0}{\pi\epsilon_0 c}} \frac{\sqrt{2}A_\omega}{\Delta\omega} e^{-r^2/s^2} \quad (4)$$

$$C_n = \left(\frac{s_0}{s}\right)^n e^{i(\psi+n\psi_G)} \quad (5)$$

$$S_n = \left(\frac{s_0}{s}\right)^n e^{i(\psi+n\psi_G+\pi/2)} \quad (6)$$

$$\psi = \Psi_0 - \frac{\omega r^2}{2cR} - \frac{\omega z}{c} - \psi_{\text{spec}} \quad (7)$$

$$\psi_{\text{spec}} = \frac{\phi_2\delta\omega^2}{2} + \frac{\phi_3\delta\omega^3}{6} + \frac{\phi_4\delta\omega^4}{24} + \dots \quad (8)$$

$$\psi_G = \tan^{-1}\left(\frac{z}{z_R}\right) \quad (9)$$

$$s = s_0 \sqrt{1 + \left(\frac{z}{z_R}\right)^2} \quad (10)$$

$$R = z + \frac{z_R^2}{z}. \quad (11)$$

P_0 is the peak power of the pulse (in this case with zero STCs), ϵ_0 is the permittivity of free space, and c is the speed of light in vacuum, however for the rest of this work we will present normalized fields since we are modeling their properties in free space only. The spectral phase parameters ϕ_2 , ϕ_3 , and ϕ_4 are the group-delay dispersion, third-order dispersion, and fourth-order dispersion respectively, included for completeness, but in our presented phenomena we will only show results with nonzero ϕ_2 . The fields above are the complex fields, where for all

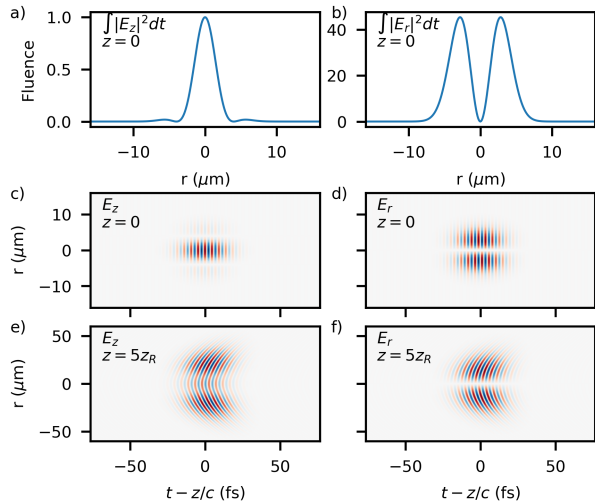


FIG. 1. Standard ultrashort RPLB in-focus with $\lambda_0 = 800$ nm, $\tau_0 = 15$ fs, and $s_0 = 4$ μm . The integrated E_z (a) is strongly localized on-axis, where the integrated E_r (b) has a zero on-axis. The E_z and E_r fields in time, (c) and (d) respectively, show similar characteristics, but as they diffract they change — shown at $z = 5z_R$ in (e) and (f) respectively. The fluence in (a) and (b) is normalized to the max fluence of E_z , and the color scale in each of panels (c)–(f) is relative to the maximum in that panel.

visualizations we show the real part of the fields in time corresponding to the physically relevant quantities.

Of course in the case of the equations above, the fields in time can be easily calculated. This is because the only frequency dependence is in the Gaussian spectral profile A_ω and the term $\omega z/c$ in the phase, so the temporal profile is simply a Gaussian envelope traveling in z at the speed of light. However, for the rest of this work we will build off of this standard case to consider pulses with non-trivial chromatic terms, which cannot be expressed simply in time, so we leave these fields in terms of frequency for reference. Because it is often the electric fields that are most important, B_θ will not generally be included in visualizations, except for in the case of spatial chirp where calculating the magnetic field requires a different coordinate transformation due to the breaking of cylindrical symmetry. It must also be noted that modeling an azimuthally-polarized laser beam requires only a simple transformation of these equations, so the work in the rest of this manuscript will also apply.

Figure 1 shows the basic characteristics of the standard ultrashort RPLB for a wavelength of 800 nm that we will use throughout this manuscript. These characteristics include the longitudinal field E_z being strongly localized on-axis and the transverse field E_r being zero on-axis, shown in Fig. 1(a) and (b) respectively, with both having cylindrical symmetry. As already mentioned, since this description does not yet contain STCs the fields are

trivially extended to having an ultrashort envelope that maintains these features in the focus, shown in Fig. 1(c)–(d). Both the monochromatic RPLB and the ultrashort RPLB become more complicated as they propagate away from the focus, shown for the ultrashort case in Fig. 1(e)–(f), still without STCs.

Note as well that the non-paraxial form could be easily constructed by adding terms of higher-order in ϵ as in Ref. [22] for example. This will also be the case for all of the models used in the following sections with STCs added, but we write only the paraxial forms for simplicity in the main text to emphasize the chromatic terms. For a more detailed discussion of the non-paraxial description see the appendix. An accurate non-paraxial description is generally believed to be necessary when the beam waist approaches the wavelength, but for highly sensitive interactions such as high-field particle acceleration a non-paraxial description becomes important even at larger beam waists [23].

III. LONGITUDINAL CHROMATISM

Longitudinal chromatism (LC) is a form of spatio-temporal coupling that is when the different spectral components of an ultrashort pulse are separated longitudinally, that is, along the direction of propagation z . In the case in this section, we model LC at the focus of an ultrashort RPLB. In fact, LC is the result of two equivalent phenomena on the collimated beam before focusing, pulse-front curvature (PFC) and chromatic curvature (CC). PFC is when the arrival time of the ultrashort pulse varies quadratically with the radius. Due to the fundamental relationship between time and frequency in light waves (via the Fourier transform), PFC is equivalent to the radius of curvature of the pulse depending linearly on frequency, which we refer to as chromatic curvature (CC). Because of this equivalence, we refer to this phenomenon on the collimated beam as CC/PFC, which is denoted by α [fs/m^2].

Because the manifestation of the near-field couplings in focus depends on the focusing geometry, the corresponding near-field beam radius can be chosen as s_i with a focal length of f , making $s_0 = 2cf/\omega_0 s_i$. However, if the collimated beam were smaller and the focal length shorter so as to have the same beam waist and Rayleigh range, then the relative effect of a certain CC/PFC α would be different. So in fact, it is the quantity $\tau_p = \alpha s_i^2$ (see Fig. 2(a)) that can properly parameterize the effect of the CC/PFC coupling regardless of the actual focusing geometry. So it is this τ_p that we use to parameterize the LC in-focus (resulting from CC/PFC on the collimated beam) for the rest of this section. The LC produces a frequency-dependent longitudinal waist position z_0 of

$$z_0 = z_R \tau_p \delta\omega, \quad (12)$$

where $\delta\omega = (\omega - \omega_0)$, i.e. describing linear LC.

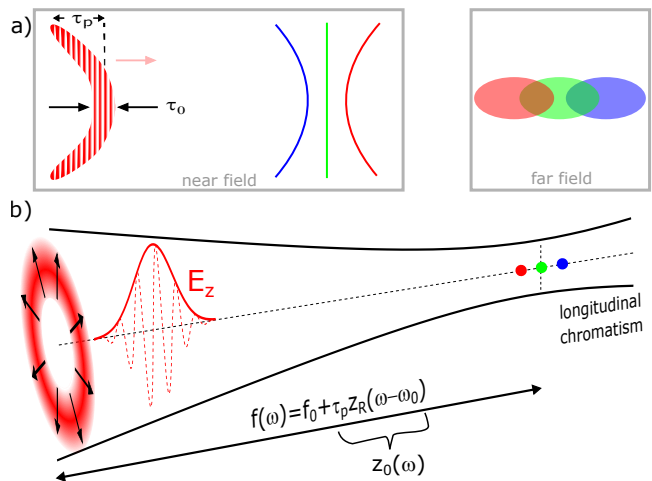


FIG. 2. Basic concept of longitudinal chromatism (LC) in the focus. A beam in the near field (a) before being focused can have pulse-front curvature (PFC) where the arrival time depends quadratically on the radius, and equivalently the frequencies have a linearly varying convergence. When focused the frequencies focus to different longitudinal positions and produce LC, shown on the right in (a). The scenario relevant for modeling the RPLB is shown schematically in (b), now with multiple components of the field.

The fields around the focus $z = 0$ are as before in Eqs.(1)–(8), but with modified terms

$$\psi_G = \tan^{-1} \left(\frac{z - z_0}{z_R} \right) \quad (13)$$

$$s = s_0 \sqrt{1 + \left(\frac{z - z_0}{z_R} \right)^2} \quad (14)$$

$$R = (z - z_0) + \frac{z_R^2}{(z - z_0)}. \quad (15)$$

We must note that the waist s_0 and Rayleigh range z_R being constant values relies on the pulses being longer than few-cycle as mentioned earlier, but in the case of LC it also relies on the difference in focal lengths between the extreme frequencies of the pulse being negligible. This is equivalent to the assumption that the extended Rayleigh range $z_R^e = \tau_p \Delta\omega z_R$ is negligible compared to the focal length f : $\tau_p \Delta\omega z_R \ll f$ or $\tau_p / \tau_0 \ll f / 2z_R$. If this were not the case, then the focal length would also need to be treated as dependent on frequency, resulting in a frequency dependence of the waist and Rayleigh range independent of the assumption of the pulse duration. After calculating the fields in frequency space with the stated assumptions, they must be inverse Fourier transformed to time.

The basic results of the model of an ultrashort RPLB with LC is shown in Figure 3 for one value of $\tau_p = 60$ fs in the focus at $z = 0$. The pulse retains cylindrical symmetry, but both E_z and E_r have much longer-tailed

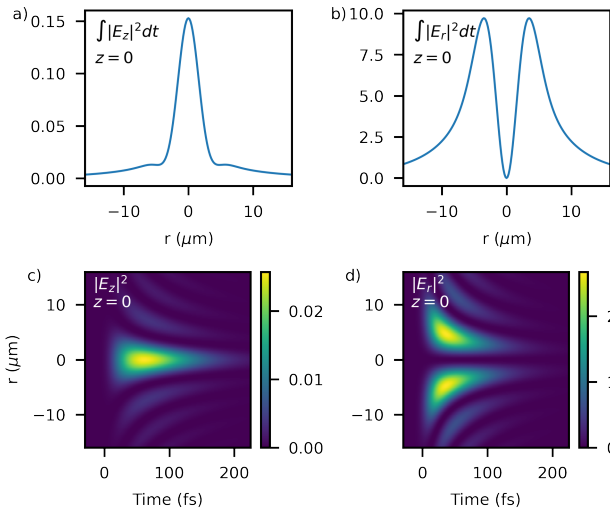


FIG. 3. Basic results with longitudinal chromatism $\tau_p = 60$ fs ($\lambda_0 = 800$ nm, $\tau_0 = 15$ fs, $s_0 = 4$ μ m). The integrated E_z and E_r fields in-focus, (a) and (b) respectively, show larger tails as r increases. The E_z and E_r fields in time, (c) and (d) respectively, now have a time asymmetry and fringes at larger r characteristic of chromaticity, but the qualitative characteristics stay the same. The fluence in (a) and (b) is normalized to the max fluence of E_z without any LC and the intensity in (c) and (d) is normalized to the max intensity of E_z without any LC.

transverse distributions, shown in Fig. 3(a)–(b). This is seen very clearly when comparing Fig. 3(a)–(b) directly to Fig. 1(a)–(b), where the only difference is the LC.

Besides the effect on the transverse profile of both polarization components, there is also a significant change in the temporal profile. As shown in Fig. 3(c)–(d) the temporal intensity profiles of both E_z and E_r are no longer symmetric in time, and have significant interference effects at the outer portions of the transverse distributions. The asymmetry and interferences are common characteristics of LC, and in this case are manifested in both polarization components, while each component maintains the basic characteristics of the ultrashort RPLB — E_z is localized on-axis and E_r is zero on-axis.

Another feature of the ultrashort RPLB with LC is an extended Rayleigh range, defined earlier as $z_R^e = \tau_p \Delta\omega z_R$. This can be simply reasoned from the fact that different colors have their waist position at different z positions. So, although the waist is larger due to the LC, the pulse retains that slightly larger waist within an increased longitudinal distance z_R^e , larger than the basic Rayleigh range by both the amount of LC τ_p and the bandwidth of the pulse $\Delta\omega$.

This increased Rayleigh range, effectively beating diffraction, has already been shown for linearly polarized pulses [24]. We confirm in Figure 4 that it is also valid for ultrashort RPLBs having LC for both E_z and E_r . Comparing Fig. 4(a)–(b) without LC to Fig. 4(c)–(d)

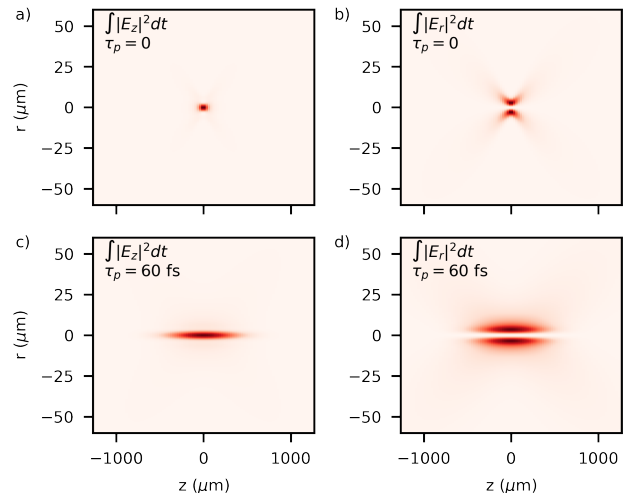


FIG. 4. Increased Rayleigh range due to the longitudinal chromatism of both the longitudinal field E_z , (a) with no LC and (c) with $\tau_p = 60$ fs, and transverse field E_r , (c) with no LC and (d) with $\tau_p = 60$ fs ($\tau_0 = 15$ fs, $s_0 = 4$ μ m).

with $\tau_p = 60$ fs the Rayleigh range is roughly $2\tau_p/\tau_0 = 8$ times larger in the latter case. What is not shown in Fig. 4(c)–(d) of course is the temporal behavior of the electric field at each z -position, as it is only showing the integrated intensity. Because the LC separates the colors then at the different points within the extended Rayleigh range the central wavelength will evolve, which can be thought of as the price paid for “beating” diffraction. Two-dimensional STC wavepackets [25, 26] have been shown to remain localized for orders of magnitude beyond the diffraction limit without separating the frequencies [27, 28], but have other limitations and are not vector beams, so can be considered a uniquely different phenomenon.

A. Flying focus effect

Longitudinal chromatism combined with linear temporal chirp (or quadratic spectral phase ϕ_2) results in the intensity of the ultrashort laser pulse traveling at velocities significantly different than c , referred to as the flying focus [19, 29]. This has been implemented with either diffractive optics [24] or specially produced lens doublets [30] to produce the LC, and has also been used to create ionization waves in a plasma at such superluminal and even negative velocities [31, 32]. Theoretical work shows potential applications in laser-plasma Raman amplification [33], plasma-based photon acceleration [34], and vacuum electron acceleration [35]. All of the past work has dealt with scalar electric fields, so we discuss and simulate the same effect with the fields of an ultrashort RPLB.

The velocity of the intensity peak in the flying focus

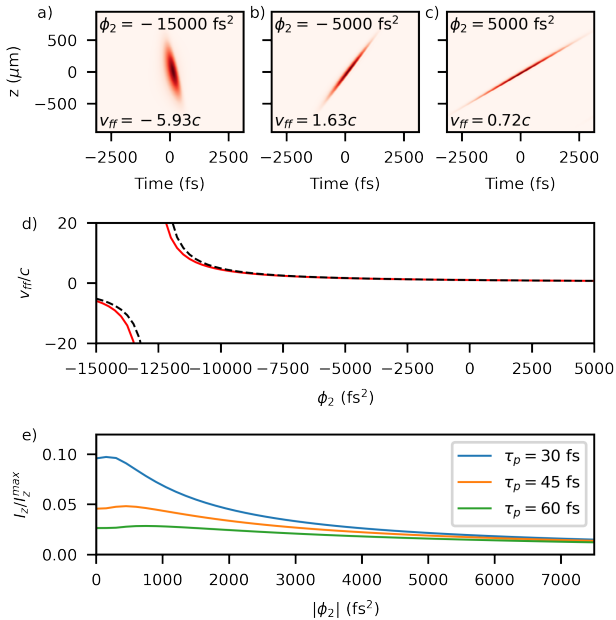


FIG. 5. Flying focus effect with the longitudinal field E_z at $r = 0$. An RPLB with an LC of $\tau_p = 60$ fs ($\tau_0 = 15$ fs, $s_0 = 4 \mu\text{m}$) is simulated with varying linear chirp (ϕ_2) to produce an intensity envelope that travels at velocities much different than c (a)–(c). The dependence of the intensity peak velocity v_{ff} on chirp (d) in the analytical equation Eq. 16 (black dashed line) agrees with the full simulations (red solid line). The intensity decreases (e) from the case with no STCs with different values of τ_p and with increasing chirp.

scenario v_{ff} has been shown to obey a simple formula [19, 29, 30]

$$\frac{v_{ff}}{c} = \frac{1}{1 + \frac{c\phi_2}{\tau_p z_R}}. \quad (16)$$

This simple formula is derived based on only the varying central frequency along the longitudinal direction and concurrent varying arrival time for the different frequencies resulting from the spectral phase. We expect that it holds similarly for the RPLB having chirp and LC since the relevant phase terms are the same.

The results for the combination of LC and chirp are shown in Figure 5 for E_z only, with $r = 0$, confirming that the flying focus phenomenon occurs as well with ultrashort RPLBs. The maps of the on-axis intensity profile for z positions through the focus is shown for E_z with a single value of $\tau_p = 60$ fs and three chirp values in Fig. 5(a)–(c). These specific combinations of LC and chirp produce negative super-luminal, positive super-luminal, and positive sub-luminal v_{ff} in Fig. 5(a), (b), and (c) respectively. The dependence of v_{ff} on the chirp from the simulations agrees very well with that predicted from the simple relationship in Eq. (16), shown in Fig. 5(d). The transition chirp where the velocity transitions from purely positive to negative occurs at roughly

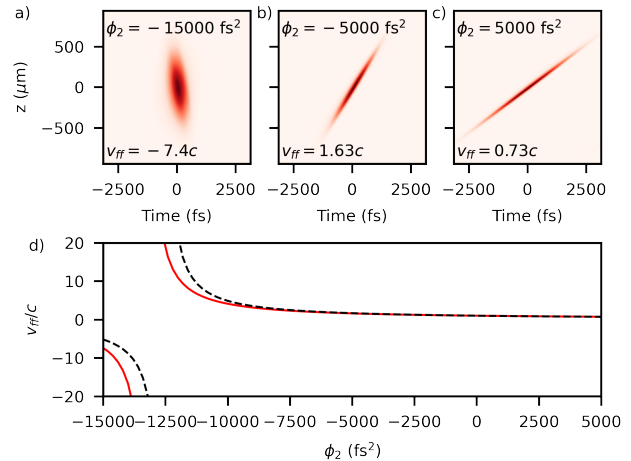


FIG. 6. Flying focus effect with the transverse field E_r at the off-axis position $r = s_0$. An RPLB with an LC of $\tau_p = 60$ fs ($\tau_0 = 15$ fs, $s_0 = 4 \mu\text{m}$) is simulated with varying linear chirp (ϕ_2) to produce an intensity envelope that travels at velocities much different than c (a)–(c), slightly different than those for E_z on-axis. The dependence on ϕ_2 (d) is slightly different in this case as well (red solid line), diverging more from the simple prediction (black dashed line) based on Eq. 16.

$\phi_2 = -\tau_p z_R/c$, the same as for linear polarization. The peak intensity of the longitudinal field decreases significantly already with the LC, and decreases further with added chirp (Fig. 5(e)), which is qualitatively similar to the intensity reduction for linear polarization [19].

The situation of LC and chirp in the transverse polarization, E_r , is more complicated both because the field is only non-zero off-axis, and because as the pulse diffracts away from the focus the position of maximum intensity is increasingly off-axis. However, as already shown in Fig. 4(d), within the extended Rayleigh range the position of maximum intensity is relatively constant. Therefore we look at the velocity of the intensity peak of E_r at $r = s_0$ ($\rho = 1$). The results for the same nonzero chirps as for E_z is shown for E_r in Fig. 6.

The result of the analysis of the flying focus off-axis with E_r is that it is only slightly different than that of E_z , both in terms of the quantitative results and the qualitative dependence on ϕ_2 . This is due to the additional phase term dependent on r in Eq. (7), the curvature term, that due to the transformation of z to $z - z_0(\omega)$ introduces a non-trivial frequency dependence when $r \neq 0$. When comparing the simulated temporal intensity profiles of E_z at $r = 0$ in Fig. 5(a)–(c) and for E_r at $r = s_0$ in Fig. 6(a)–(c), the results are therefore slightly different. However, this is most apparent around the transition chirp. For example with $\phi_2 = -15000$ fs² the velocity is $-5.93c$ for E_z on-axis and $-7.4c$ for E_r off-axis. The difference in the dependence on the chirp is seen clearly in Fig. 6(d) near the transition chirp of -12500 fs² when compared to Fig. 5(d). It is interesting that the phase term due to curvature is in the phase both for E_z and E_r , meaning that

as r increases the velocity changes for E_z as well, which we have confirmed via numerical calculations, but this difference is less important for E_z because the intensity decreases rapidly off-axis.

As a last observation, both for E_z and E_r , producing a changing velocity (i.e. accelerating, decelerating, or non-monotonic) of the intensity peak is also possible with higher orders of spectral phase ϕ_3 , ϕ_4 , etc. as already predicted for linear polarization [19].

It is important again to emphasize the difference from STC wavepackets [26] that have been shown as well to have tunable velocities [36–38]. The flying focus shown here, besides being with a cylindrical vector beam, is limited to a region around the focus defined by z_R^c and the different frequencies of the initial laser pulse are separated longitudinally within that region. Therefore, the flying focus for both linear polarization and with ultrashort RPLBs is most relevant to phenomena that are purely intensity-dependent, otherwise this separation of the frequencies must be taken into account. The tunable velocity STC wavepackets, shown so far only for linear polarization, do not have the separation of frequencies and can have localized propagation orders of magnitude longer than as predicted by diffraction, but for reasons already discussed can be considered significantly different than the case discussed in this manuscript. Besides these STC wavepackets, more complex examples with programmable group velocities involving Bessel beams have recently been described [39], which could also theoretically be adapted to RPLBs.

IV. SPATIAL CHIRP

In this section we model spatial chirp in the focus of an RPLB. Spatial chirp around the focus is due to angular-dispersion (AD) in the near-field, where different frequencies have different pointing directions, or equivalently the pulse-front of the beam is tilted from the wavefront (pulse-front tilt, PFT), see Fig. 7(a). Because these are equivalent, it can be referred to as AD/PFT to be unambiguous. When focused the different pointing directions of different frequencies result in the frequencies being spatially separated in the focal region, as in Fig. 7(b), along the axis where there was AD/PFT in the near field. This transverse spatial separation of frequencies is exactly spatial chirp (SC).

As it was with LC, the in-focus manifestation of the near-field AD/PFT—represented by the tilt angle $\eta = dt/dx$ [fs/m]—depends on the focusing geometry. So, similar to the case of LC it is the time delay at the outer edge of the near field (with beam size s_i) due to AD/PFT $\tau_t = \eta s_i$ (see Fig. 7(a)) that can properly parameterize the effect of the near-field AD/PFT coupling regardless of the actual focusing geometry. So it is this τ_t that we use to parameterize the SC in-focus (resulting from AD/PFT on the collimated beam) for the rest of this section. Linear SC is described by a best-focus position

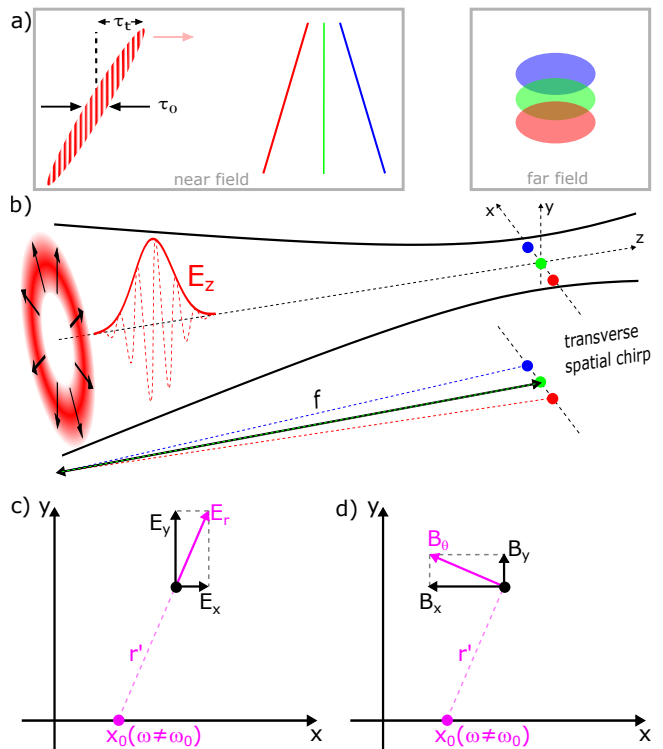


FIG. 7. Basic concept of spatial chirp (SC) in the focus. A beam in the near field (a) before being focused can have pulse-front tilt (PFT) where the arrival time depends linearly on one spatial coordinate, and equivalently the frequencies have a linearly varying pointing direction, or angular dispersion (AD). When focused (b) the frequencies separate along the same axis as the AD/PFT and produce spatial chirp (SC). Due to the breaking of cylindrical symmetry both E_r and B_θ require a frequency-dependent transformation to cartesian coordinates, shown in (c) and (d) respectively.

x_0 of

$$x_0 = s_0 \tau_t \delta \omega / 2, \quad (17)$$

which is clearly linear in frequency and proportional to τ_t representing the AD/PFT.

The key difference between the modeling of SC is that there is no longer cylindrical symmetry as in the previous section. This is because with AD/PFT on the collimated beam, the different frequencies are focused to different positions along one transverse axis, chosen to be x here (see Fig. 7(b)). This not only affects the spectral content at any given position, but it affects the direction of the fields, which depends non-trivially on frequency.

The implication is that the initial fields \tilde{E}_r , \tilde{E}_z , and \tilde{B}_θ must be transformed to Cartesian coordinates, and all fields \tilde{E}_x , \tilde{E}_y , \tilde{E}_z , \tilde{B}_x , and \tilde{B}_y ($\tilde{B}_z = 0$ still) must be calculated at all x , y , and z positions. However, because the frequencies are shifted a different amount along x in the focal plane, the coordinate transformation is also frequency dependent. This concept is sketched in Fig. 7(c)

for \tilde{E}_r and in Fig. 7(d) for \tilde{B}_θ . The results are:

$$\tilde{E}_x(\omega) = \tilde{E}_r(\omega, r') \left(\frac{x - x_0}{r'} \right) \quad (18)$$

$$\tilde{E}_y(\omega) = \tilde{E}_r(\omega, r') \left(\frac{y}{r'} \right) \quad (19)$$

$$\tilde{B}_x(\omega) = \tilde{B}_\theta(\omega, r') \left(\frac{-y}{r'} \right) \quad (20)$$

$$\tilde{B}_y(\omega) = \tilde{B}_\theta(\omega, r') \left(\frac{x - x_0}{r'} \right), \quad (21)$$

where $r' = \sqrt{(x - x_0)^2 + y^2}$. The \tilde{E}_z field does not require any transformation, but it is still distributed along x according to x_0 .

As before we use pulses that have Gaussian spatial and temporal profiles, with characteristic widths s_0 and τ_0 respectively, at a central wavelength λ_0 ($\omega_0 = 2\pi c/\lambda_0$). The fields of the focused RPLB with SC are modeled similarly in the frequency domain as in Ref. [19, 20] and the previous sections. We first must simply have the new frequency dependent coordinate $\rho' = r'/s_0 = \sqrt{(x - x_0)^2 + y^2}/s_0$. However a more complicated step is to apply the transformation to Cartesian coordinates together with the amplitude modifications from Eqs. (18)–(21) resulting in

$$\tilde{E}_x(\omega) = A_{SC} C_2 \frac{(x - x_0)}{z_R} \quad (22)$$

$$\tilde{E}_y(\omega) = A_{SC} C_2 \frac{y}{z_R} \quad (23)$$

$$\tilde{E}_z(\omega) = A_{SC} \epsilon^2 [S_2 - \rho'^2 S_3] \quad (24)$$

$$\tilde{B}_x(\omega) = -A_{SC} C_2 \frac{y}{cz_R} \quad (25)$$

$$\tilde{B}_y(\omega) = A_{SC} C_2 \frac{(x - x_0)}{cz_R}, \quad (26)$$

where C_n and S_n are as in Eqs. (5)–(6), with the modified r' replacing r in the amplitude and phase:

$$A_{SC} = \frac{\omega_0}{2c} \sqrt{\frac{8P_0}{\pi\epsilon_0 c}} \frac{\sqrt{2}A_\omega}{\Delta\omega} e^{-r'^2/s^2} \quad (27)$$

$$\psi = \Psi_0 - \frac{\omega r'^2}{2cR} - \frac{\omega z}{c} - \psi_{\text{spec}}. \quad (28)$$

After calculating the fields in frequency space they must be inverse Fourier transformed to time as before.

The first most basic result is shown in Fig. 8 via the fluence of the different polarization components with a single value of τ_t at the focus $z = 0$. The simulated data is shown to replicate what would be seen on a camera when rejecting orthogonal polarizations in Fig. 8(a)–(b), and shows only the longitudinal component in Fig. 8(c). The total intensity shown in Fig. 8(d) replicates what would be seen on a standard camera with no analysis optics.

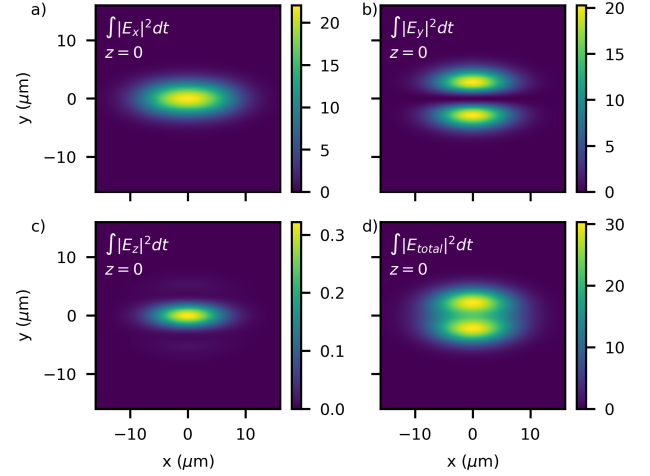


FIG. 8. The intensity of the different electric field components (a) $|E_x|^2$ (b) $|E_y|^2$, and (c) $|E_z|^2$ are shown with an SC in the x -direction of $\tau_t = 30$ fs ($\lambda_0 = 800$ nm, $\tau_0 = 15$ fs, $s_0 = 4$ μ m). These show the asymmetry and elongation along x due to the SC. The total intensity (d), which one would see on a standard camera, is also elongated along x and is asymmetric. The fluence in all panels is normalized to the max fluence of E_z without any STC.

The qualitative results of Fig. 8 agree with our expectations that with SC along x , E_y and E_z will be simply elongated along x . However, non-trivially, E_x is extended along x but also loses its zero at $x = y = 0$, seen in Fig. 8(a). Therefore not only is the total electric field in Fig. 8(d) extended along x , but it has more nuanced asymmetries and no longer a polarization singularity on axis at $x = y = 0$.

However, beyond the simple asymmetry, there are effects on the temporal evolution of the electric field and the intensity that have potential applications and require a closer look.

A. Wavefront rotation

Wavefront rotation is a phenomenon with many applications with linearly-polarized laser pulses [40] including the attosecond lighthouse technique for generating isolated attosecond pulses [41–44]. The wavefront rotation, defined as a changing wavefront plane in time at one point in a laser pulses propagation, is a result of SC in a focus.

Mathematically, if we follow the definition of Ref. [44], the angle of the wavefront is $\beta = (\partial\phi(x, t)/\partial x)(c/\omega_0)$ and the rate of change of this angle, the WFR velocity $v_r = d\beta/dt$ [rad/s], for a linearly polarized pulse is

$$v_r^{(1p)} = \frac{c\tau_t}{2\omega_0 s_0} \frac{\Delta\omega^2}{1 + (\tau_t \Delta\omega/2)^2}, \quad (29)$$

with $z = y = 0$ and using the notation of this

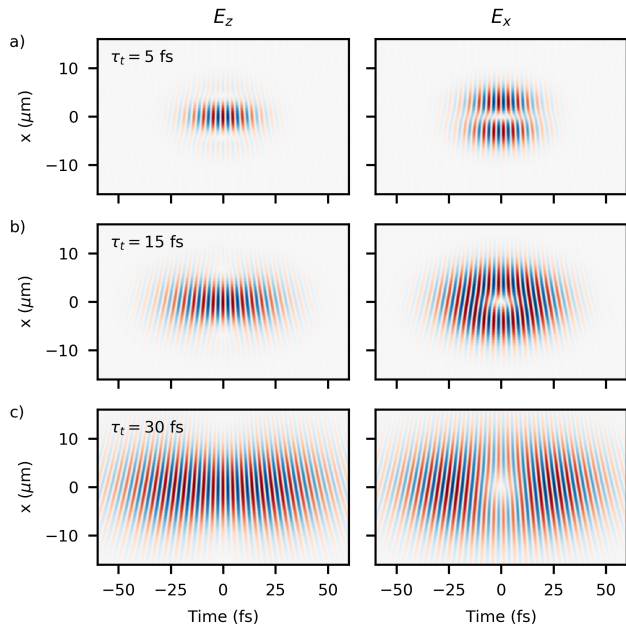


FIG. 9. Varying wavefront rotation (WFR) with different spatial chirp values, parametrized by τ_t , of (a) 5 fs, (b) 15 fs, and (c) 30 fs ($\tau_0 = 15$ fs, $s_0 = 4 \mu\text{m}$). The WFR is clearly visible and increasing in E_z (left), but is less clear in E_x (right), discussed in more detail in the text.

manuscript.

It can be shown that this WFR velocity can be calculated directly from the fields in frequency space using the mean frequency $\bar{\omega}$ (which depends on the transverse coordinate x in the case of SC) such that $v_r = (\partial\bar{\omega}/\partial x)(c/\omega_0)$. This results in exactly the same relationship for RPLBs as that in Ref. [44] and Eq.(29) for linearly polarized pulses.

Being able to calculate this WFR velocity using only frequency-space intuition is helpful for this work since we model the ultrashort RPLB field in frequency space. However, additional terms in the spectral amplitude for E_z and E_r mean that the WFR velocity will have a transverse dependence and the meaning of it will be more complicated due to the minima in the intensity. Rather than doing this calculation we visualize the WFR.

Figure 9 shows the resulting WFR in the case of E_z and E_x for three values of τ_t . One can see complexities in both E_z and E_x . For example, the WFR in E_z dislocates briefly near the off-axis intensity minima (see left of Fig. 9). The WFR of E_x also dislocates near the axis, where there are also intensity minima (see right of Fig. 9). Away from the axis for E_x and away from the off-axis intensity minima for E_z the WFR velocity is roughly uniform corresponding to Eq.(29). Note as well the on-axis field and amplitude is significantly modified, with a longer pulse for both E_z and E_x as expected, but also temporal structure in E_x .

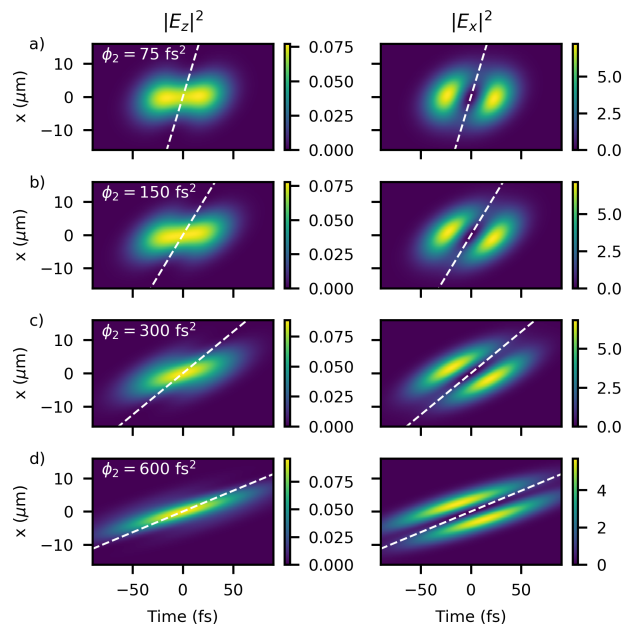


FIG. 10. Adding linear chirp (nonzero ϕ_2) to an RPLB having SC can lead to in-focus pulse-front tilt of a different nature than standard AD/PFT on a collimated beam. This is shown with $\tau_t = 30$ fs on all beams and an increasing chirp of (a) 75 fs², (b) 150 fs², (c) 300 fs², and (d) 600 fs² ($\tau_0 = 15$ fs, $s_0 = 4 \mu\text{m}$). The PFT manifests in both $|E_z|^2$ (left) and $|E_x|^2$ (right). The white dashed lines are the PFT predicted by Eq. (30). The intensity in all panels is normalized to the max intensity of E_z without any STC.

B. Pulse-front tilt

A beam that has linear SC combined with linear temporal chirp (quadratic spectral phase or group-delay dispersion, GDD, ϕ_2) also has pulse-front tilt [45]. This is simply due to the fact that the frequencies are distributed along one spatial axis and the arrival time is also linearly dependent on frequency. This is pulse-front tilt of a different nature than AD/PFT on the collimated beam as described earlier, and since we are now looking in the focus the transverse dimension is rather s_0 .

The central frequency of a linearly polarized pulse has the same behavior as in the previous section such that $\bar{\omega}(x) = \omega_0 + x\zeta$. The temporal phase is in general not linearly dependent on the GDD ϕ_2 , but if we assume that the chirp is large, $\phi_2\Delta\omega^2 \gg 2$, then $\bar{\omega}(t) = \omega_0 + t/\phi_2$. This results in a pulse-front tilt $\eta = dt/dx = \phi_2\zeta$ [s/m] of

$$\eta = \frac{\tau_t\phi_2}{2s_0} \frac{\Delta\omega^2}{1 + (\tau_t\Delta\omega/2)^2}, \quad (30)$$

which for linearly-polarized pulses is accurate with the stated assumption of large chirp.

However, as was the case with WFR, the PFT is also

influenced by the more complicated off-axis spectral envelope of the RPLB such that Eq. (30) is not fully accurate. Figure 10 shows the developing tilt at $z = 0$ for a single value of $\tau_t = 30$ fs as the chirp is increased, for both $|E_z|^2$ and $|E_x|^2$. The agreement with Eq. (30) improves as the chirp is increased, seen clearly comparing Fig. 10(a) and Fig. 10(d). The agreement for $|E_z|^2$ is still not great when $\phi_2 = 600$ fs², Fig. 10(d), however for $|E_x|^2$ the agreement is very good despite the more complicated temporal intensity profile. Note counter-intuitively that the peak intensity of E_z is not decreasing as chirp is added in the left column of Fig. 10, and is in fact slightly increasing. We confirm that beyond 600 fs² the peak intensity does begin to decrease for the specific parameters of Fig. 10, and that for larger values of τ_t the peak intensity is maximum at a larger chirp. This interesting result potentially allows for designed aberrations with a partially mitigated intensity decrease.

V. FREQUENCY-DEPENDENT BEAM PARAMETERS

In the previous two models the beam width and Rayleigh range have been approximated as constant values related to the central frequency and the pulse duration was such that the RPLB with no STCs had many cycles. However, diffraction itself and especially tight focusing is a chromatic phenomenon, and therefore the waist and Rayleigh range are in reality frequency dependent properties: $z_R = \omega s_0^2/2c$ is a fixed relationship where either z_R or s_0 can have frequency dependence according to the specifics of the physical situation. This phenomenon was known early on to effect the reshaping of single-cycle pulses through the focus [46–49]. The detailed effect of a non-uniform spatio-spectral beam width on the phase in the focus of ultrashort pulses—the so-called focal-phase—has been explored in-depth with linearly-polarized pulses [50–53] and shown to have an effect on photoelectron production driven by such ultrashort laser pulses [54, 55]. A model with RPLBs, similar to that presented here, was used to show that the effect is significant as well in vacuum laser acceleration [21].

The basics of the model are first that Eqs. (1)–(11) for the standard RPLB are modified with frequency-dependent Rayleigh range $z_R(\omega)$ and waist $s_0(\omega)$. In order to encapsulate the frequency dependence we use the “Porras factor” g_0 :

$$g_0 = -\left. \frac{dz_R(\omega)}{d\omega} \right|_{\omega_0} \frac{\omega_0}{z_R(\omega_0)}. \quad (31)$$

We use the reference parameter of the beam waist at the central frequency $s_0(\omega_0) = s_{00}$, which results in the equations for the beam parameters

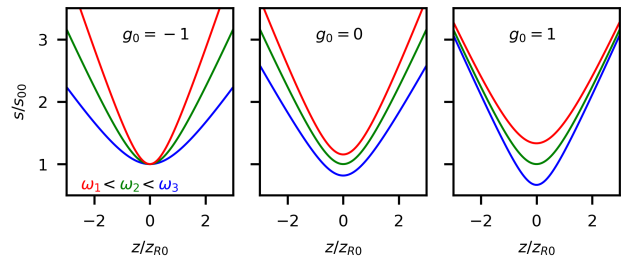


FIG. 11. The basic concept of g_0 shown with three frequencies and three g_0 values. When $g_0 = -1$ (left) all frequencies have the same beam size in the focus, where in contrast when $g_0 = 1$ (right) all three frequencies diverge with the same opening angle outside of the focus. $g_0 = 0$ (middle) is an intermediate situation.

$$z_R(\omega) = z_{R0} \left(\frac{\omega_0}{\omega} \right)^{g_0} = \frac{\omega_0 s_{00}^2}{2c} \left(\frac{\omega_0}{\omega} \right)^{g_0} \quad (32)$$

$$s_0(\omega) = s_{00} \left(\frac{\omega_0}{\omega} \right)^{\frac{g_0+1}{2}}. \quad (33)$$

This is shown for three frequencies in the case of $g_0 = -1, 0,$ and 1 in Fig. 11.

In order for the effects of the frequency-dependent parameters to be significant, the temporal duration must approach just a few optical cycles. In this regime the Gaussian spectral envelope is no longer strictly valid. We use a Poisson-like spectrum as follows

$$A_\omega(\omega) = \sqrt{\frac{2}{\pi}} \left(\frac{\gamma\omega}{\omega_0} \right)^{\gamma+1} \left(\frac{1}{\omega} \right) \frac{e^{-\gamma\omega/\omega_0}}{\Gamma(\gamma+1)}, \quad (34)$$

where γ is the parameter that now represents the pulse duration, with $\tau_0 = \gamma\sqrt{e^{2/(\gamma+1)}} - 1/\omega_0$ ($1/e^2$ intensity width) [56], and $\Gamma(\dots)$ is the Gamma function for the purely real argument $\gamma + 1$.

Using these frequency-dependent parameters (Eqs. (32)–(33)) and Poisson-like spectral envelope (Eq. (34)) in place of the relevant terms in Eqs. (1)–(11), and Fourier transforming to time, produces the fields without the common frequency-independent approximation.

The main result of properly modeling the frequency-dependent beam parameters is that the carrier-envelope phase (CEP) varies through the focus in a way non-trivially different than the standard Guoy phase. The key difference with the RPLB is that this behavior is not the same for the different polarization components. The CEP evolution $\Delta\Psi$ through the focus is calculated using the relation $\Delta\Psi = \phi|_{\omega_0} - \omega_0 \frac{\partial\phi}{\partial\omega}|_{\omega_0}$ (the difference between the pulse-front and the wavefront) where ϕ is the total phase such that

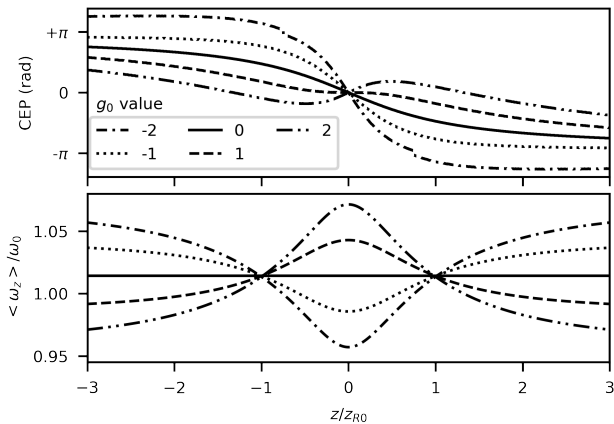


FIG. 12. On-axis CEP and central frequency evolution through the focus with a duration of 3.5 fs ($\gamma=35$). The CEP (top) varies widely, showing a steep slope at $g_0 = -2$ and an inflection when $g_0 \geq 1$. The central frequency (bottom) also varies through the focus due to the reshaping of the frequency envelope as different frequencies are focused more tightly. This figure is identical to one presented in ref. [21].

$$\Delta\Psi_r(r, z) = \frac{g_0 \left[2 - 2\frac{r^2}{s^2} \right]}{\frac{z}{z_{R0}} + \frac{z_{R0}}{z}} - 2 \tan^{-1} \left(\frac{z}{z_{R0}} \right) \quad (35)$$

$$\Delta\Psi_z(r=0, z) = \Delta\Psi_r(r=0, z). \quad (36)$$

Note that s is the usual frequency-independent value as in Eq. 10 and the last term in Eq. (35) is simply double the frequency-independent Gouy phase as in Eq. 9. Due to the complexity of the phase for $E_z(r \neq 0, z)$, the expression for the CEP evolution is not solved for explicitly in that case except for when $r = 0$, where it is in fact equal to that of E_r .

Besides the CEP evolution through the focus, the central frequency also evolves. This is easy to visualize since, as depicted in Fig. 11, the different colors are focused to different waists depending on the g_0 value. Regardless of the assumed integrated spectral envelope A_ω , the central frequency must evolve through the focus since the colors that are larger outside of the focus are the smallest within the focus and vice-versa.

The on-axis ($r = 0$) CEP evolution, identical for E_r and E_z as in Eq. (36), is shown in Fig. 12(top), and the central frequency evolution for E_z is shown in Fig. 12(bottom) for $\tau_0 = 3.5$ fs ($\gamma=35$). It is important to note that the CEP evolution does not change with the pulse duration, it only has a greater significance as the pulse duration decreases, but the central frequency evolution does depend strongly on the pulse duration [50].

These on-axis results in Fig. 12 were already reported in the context of the application to vacuum acceleration of electrons [21]. However, the off-axis CEP evolution has not yet been reported and is shown here in Fig. 13 for E_z and E_r for both $g_0 = -1$ and $+1$. The plotted results

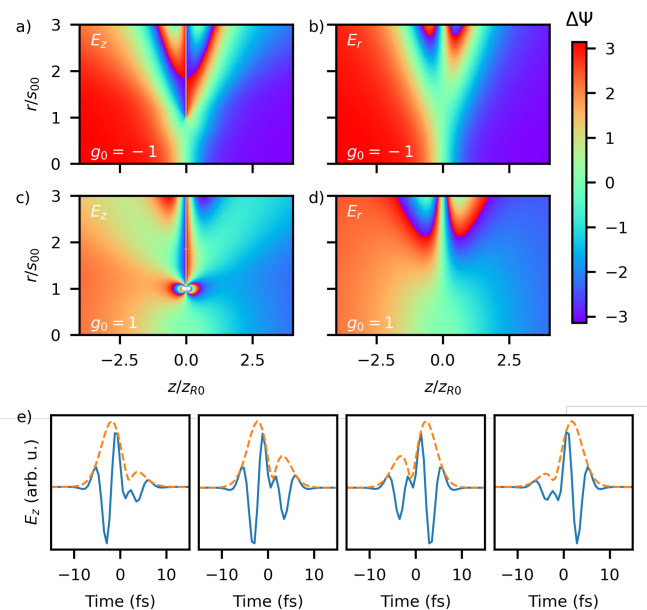


FIG. 13. Off-axis CEP evolution through the focus. The CEP for both E_z ((a) and (c)) and E_r ((b) and (d)) are shown through the focus for on- and off-axis positions, with a g_0 of -1 ((a) and (b)) and $+1$ ((c) and (d)). The discontinuities in the CEP of E_z are due to pulse reshaping around $r/s_{00} = 1$ and $z = 0$, shown in (e) for a pulse duration of 3.5 fs ($\gamma=35$) with $g_0 = 1$ at four z/z_{R0} positions of $-1/4, -1/8, +1/8, +1/4$ from left to right, with the field (blue solid line) and the amplitude (orange dashed line).

for E_r are simply that of Eq. (35), while the results for E_z are calculated via the numerical differentiation of the phase of the field.

The first result to note is that the difference between the phase for varying g_0 clearly extends to off-axis positions as well both for E_z and E_r , most clear when comparing off-axis positions in Fig. 13(b) to Fig. 13(d). The second notable result is that for E_z there are significant discontinuities as r increases. Specifically at $r/s_{00} = 1$ and $z = 0$ the discontinuity is due to local reshaping of the field as shown in Fig. 13(e), which exposes a weakness of the simple method to calculate the CEP change. One could extend the analysis away from the implicit non-reshaping assumption as in Ref. [51], but in this specific region E_z becomes very small and is therefore less important, and due to the very significant reshaping the meaning of the CEP is less clear. We therefore leave a more nuanced analysis to a further work.

VI. CONCLUSION

We have presented the fields of ultrashort radially-polarized laser pulses when tightly focused and having three different low-order spatio-temporal couplings: longitudinal chromatism, spatial chirp, and frequency-dependent beam parameters. We presented results

mostly directly in the focus but also included some propagation characteristics. This was presented for all three cases using a model where the effect of the STCs was developed by adding frequency-dependence to parameters of the description in frequency-space and confirming the existence of important effects in the time domain via numerical Fourier transformation. The lack of an analytical description directly in the time domain is an important aspect of ongoing work, and we hope that drawing upon the descriptions of other fundamental ultrashort pulses that have interesting space-time properties such as tilted beams [57], the flying donut [58–60], or the previously mentioned space-time light sheets [26] may address this issue. Still, we believe that developing this model and recipe for describing low-order STCs and showing the powerful effects that take place in the focus of ultrashort radially-polarized laser beams is useful without the time domain equations.

Further complexities can be imagined beyond what was presented in this manuscript. The first possibility of course is including higher-order STCs, such as LC or SC that are nonlinearly dependent on the frequency or frequency-dependent beam width that cannot be described by one parameter, or indeed a simple combination of the presented STCs. Or, for example, combining the presented STCs with more realistic near-field profiles for high-power laser beams such as the super-Gaussian or flattened-Gaussian [61], or modelling higher-order vector beams, or using the Richards–Wolf formalism [62, 63] to model very non-paraxial beams or beams diffracting from an aperture, important for the Guoy phase of RPLBs [64]. Additionally, there may be nuanced behavior of either the phase or the electric field when including a more detailed analysis of the RPLBs outside of the focus. The models presented here are general and provide the framework for investigating these more complex situations.

We believe that the combination of vector beams and STCs will become of increasing interest for ultrafast optical applications as the knowledge and understanding becomes more advanced. The combination of the models and analysis presented in this work and the further development of methods to control and characterize STCs [65]—also for vector beams [66]—will enable this advancement.

ACKNOWLEDGEMENTS

Example scripts to generate the fields presented in this work are available in a public repository [67].

The author would like to acknowledge Fabien Quéré for helpful discussions and Martin Virte for input on the manuscript.

APPENDIX: NON-PARAXIAL DESCRIPTION

Here we outline the description for non-paraxial beams according to the method used in Ref. [22] to add to the paraxial equations and results presented in the main text. The chosen method, without STCs, expands the wave equation to higher orders of the generally small parameter $\epsilon = s_0/z_R = \lambda_0/\pi s_0$ to have more accurate descriptions of the fields, improving upon Eqs. 1–3, with all of the same properties unchanged from Eqs. 5–11. Specifically,

$$\begin{aligned} \tilde{E}_r = A_{\text{np}} \left\{ \epsilon [\rho C_2] + \epsilon^3 \left[-\frac{\rho C_3}{2} + \rho^3 C_4 - \frac{\rho^5 C_5}{4} \right] \right. \\ \left. + \epsilon^5 \left[-\frac{3\rho C_4}{8} - \frac{3\rho^3 C_5}{8} + \frac{17\rho^5 C_6}{16} - \frac{3\rho^7 C_7}{8} + \frac{\rho^9 C_8}{32} \right] \right\} \end{aligned} \quad (37)$$

$$\begin{aligned} \tilde{E}_z = A_{\text{np}} \left\{ \epsilon^2 [S_2 - \rho^2 S_3] \right. \\ \left. + \epsilon^4 \left[\frac{S_3}{2} + \frac{\rho^2 S_4}{2} - \frac{5\rho^4 S_5}{4} + \frac{\rho^6 S_6}{4} \right] \right\} \end{aligned} \quad (38)$$

$$\begin{aligned} \tilde{B}_\theta = \frac{A_{\text{np}}}{c} \left\{ \epsilon [\rho C_2] + \epsilon^3 \left[\frac{\rho C_3}{2} + \frac{\rho^3 C_4}{2} - \frac{\rho^5 C_5}{4} \right] \right. \\ \left. + \epsilon^5 \left[\frac{3\rho C_4}{8} + \frac{3\rho^3 C_5}{8} + \frac{3\rho^5 C_6}{16} - \frac{\rho^7 C_7}{4} + \frac{\rho^9 C_8}{32} \right] \right\}. \end{aligned} \quad (39)$$

The only additional correction is on the beam power, of the form

$$A_{\text{np}} = \frac{\omega_0}{2c} \sqrt{\frac{8P_{\text{np}}}{\pi\epsilon_0 c}} \frac{\sqrt{2}A_\omega}{\Delta\omega} e^{-r^2/s^2} \quad (40)$$

$$P_{\text{np}} = \frac{P_0}{1 + 3\left(\frac{\epsilon}{2}\right)^2 + 9\left(\frac{\epsilon}{2}\right)^4}, \quad (41)$$

where P_0 is the physical power of the beam, equal to the power in the non-paraxial case (without STCs). It must be noted that while this description is more accurate in describing the fields for moderate values of ϵ , the convergence is not well understood as ϵ becomes comparable to 1 since it is based on an expansion in ϵ as a small parameter.

When longitudinal chromatism (LC) is present z is replaced everywhere with $z - z_0(\omega)$ which effects the same terms ψ_G , s , and R as in Eqs. 13–15. This results in both the amplitude and phase of all C_n and S_n being frequency dependent, with the only difference being that in the non-paraxial case there are many more terms of higher n .

In the case where spatial chirp (SC) is present the modifications are also as before in the paraxial case, effecting

the amplitude of all of the fields as in Eq. 27 and the phase as in Eq.28 due to the modified r' , and also requiring a frequency-dependent coordinate transformation as in Eqs. 18–21. The main difference then for the non-paraxial case is the higher orders of ρ that now need to be described by the frequency-varying ρ' , and as for LC the phase effects are present as well in the higher orders of C_n and S_n .

For the third and final STC described in the main text, frequency-varying beam parameters, z_R and s_0 need to be replaced by their frequency-dependent form depending on the g_0 value as in Eqs. 32–33. This introduces frequency dependence in ϵ , ρ , s , ψ_G , and R which in sum effect both the phase and amplitude. And again, the primary additional complexity in the non-paraxial case is the higher orders present of ϵ , ρ , C_n , and S_n .

In summary, the non-paraxial equations have been presented in this appendix and a recipe for adapting each

of the three STCs presented in the main text to the non-paraxial form has been given here. However, this could only be in a general matter since in all cases both the amplitude and phase develop frequency dependence that is of much higher order in the non-paraxial form and therefore non-trivial. It must be noted that for the parameters presented in the main text ($\lambda_0=800$ nm, $s_0=4$ μ m, $\epsilon=0.0637$) the non-paraxial results are qualitatively the same, confirmed by numerical calculations, and the fields and intensity are very similar quantitatively. Only for extremely sensitive interactions such as vacuum electron acceleration would the non-paraxial fields be important with such focusing [23]. Indeed for tighter focusing (larger ϵ) the non-paraxial form becomes more important, and would begin to significantly effect especially the field-based effects presented in the main text, specifically wavefront rotation and the changing CEP through the focal volume.

-
- [1] S. Quabis, R. Dorn, M. Eberler, O. Glöckl, and G. Leuchs. Focusing light to a tighter spot. *Optics Communications*, 179:1–7, 2000.
- [2] R. Dorn, S. Quabis, and G. Leuchs. Sharper focus for a radially polarized light beam. *Physical Review Letters*, 91(23):233901, 2003.
- [3] C. J. R. Sheppard and A. Choudhury. Annular pupils, radial polarization, and superresolution. *Applied Optics*, 43(22):4322–4327, 2004.
- [4] F. Lu, W. Zheng, and Z. Huang. Coherent anti-stokes raman scattering microscopy using tightly focused radially polarized light. *Optics Letters*, 34(12):1870–1872, 2009.
- [5] Y. Kozawa, T. Hibi, A. Sato, H. Horanai, M. Kurihara, N. Hashimoto, H. Yokoyama, T. Nemoto, and S. Sato. Lateral resolution enhancement of laser scanning microscopy by a higher-order radially polarized mode beam. *Optics Express*, 19(17):15947–15954, 2011.
- [6] Q. Zhan. Trapping metallic rayleigh particles with radial polarization. *Optics Express*, 12(15):3377–3382, 2004.
- [7] H. Kawauchi, K. Yonezawa, Y. Kozawa, and S. Sato. Calculation of optical trapping forces on a dielectric sphere in the ray optics regime produced by a radially polarized laser beam. *Optics Letters*, 32(13):1839–1841, 2007.
- [8] Y. Kozawa and S. Sato. Optical trapping of micrometer-sized dielectric particles by cylindrical vector beams. *Optics Express*, 18(10):10828–10833, 2010.
- [9] Lu Huang, Honglian Guo, Jiafang Li, Lin Ling, Baohua Feng, and Zhi-Yuan Li. Optical trapping of gold nanoparticles by cylindrical vector beam. *Optics Letters*, 37(10):1694–1696, 2012.
- [10] C. Varin, M. Piché, and M. A. Porras. Acceleration of electrons from rest to GeV energies by ultrashort transverse magnetic laser pulses in free space. *Physical review E*, 71:026603, 2005.
- [11] P.-L. Fortin, M. Piché, and C. Varin. Direct-field electron acceleration with ultrafast radially polarized laser beams: scaling laws and optimization. *Journal of Physics B: Atomic, Molecular and Optical Physics*, 43:025401, 2010.
- [12] L. J. Wong and F. X. Kärtner. Direct acceleration of an electron in infinite vacuum by a pulsed radially-polarized laser beam. *Optics Express*, 18(24):25035–25051, 2010.
- [13] S. Payeur, S. Fourmaux, B. E. Schmidt, J. P. MacLean, C. Tchervenkov, F. Légaré, M. Piché, and J. C. Kieffer. Generation of a beam of fast electrons by tightly focusing a radially polarized ultrashort laser pulse. *Applied Physics Letters*, 101:041105, 2012.
- [14] S. Carbajo, E. A. Nanni, L. J. Wong, G. Moriena, P. D. Keathley, G. Laurent, R. J. D. Miller, and F. X. Kärtner. Direct longitudinal laser acceleration of electrons in free space. *Physical Review Accelerators and Beams*, 19:021303, 2016.
- [15] L. J. Wong, K.-H. Hong, S. Carbajo, A. Fallahi, P. Piot, M. Soljačić, J.D. Joannopoulos, F. X. Kärtner, and I. Kaminer. Laser-induced linear-field particle acceleration in free space. *Scientific Reports*, 7:11159, 2017.
- [16] P. Dombi, Z. Pápa, J. Vogelsang, S. V. Yalunin, M. Sivis, G. Herink, S. Schäfer, P. Groß, C. Ropers, and C. Lienau. Strong-field nano-optics. *Reviews of Modern Physics*, 92:025003, 2020.
- [17] S. Akturk, X. Gu, P. Bowlan, and R. Trebino. Spatio-temporal couplings in ultrashort laser pulses. *Journal of Optics*, 12:093001, 2010.
- [18] C. Bourassin-Bouchet, M. Stephens, S. de Rossi, F. Delmotte, and P. Chavel. Duration of ultrashort pulses in the presence of spatio-temporal coupling. *Optics Express*, 19(18):17357–17371, 2011.
- [19] A. Sainte-Marie, O. Gobert, and F. Quéré. Controlling the velocity of ultrashort light pulses in vacuum through spatio-temporal couplings. *Optica*, 4(10):1298–1304, 2017.
- [20] S. W. Jolly. Influence of longitudinal chromatism on vacuum acceleration by intense radially polarized laser beams. *Optics Letters*, 44(7):1833–1836, 2019.
- [21] S. W. Jolly. On the importance of frequency-dependent beam parameters for vacuum acceleration with few-cycle radially-polarized laser beams. *Optics Letters*, 45(14):3865–3868, 2020.
- [22] Y. I. Salamin. Fields of a radially polarized Gaussian laser beam beyond the paraxial approximation. *Optics Letters*, 31(17):2619–2621, 2006.

- [23] V. Marceau, C. Varin, and M. Piché. Validity of the paraxial approximation for electron acceleration with radially polarized laser beams. *Optics Letters*, 38(6):821–823, 2013.
- [24] D. H. Froula, D. Turnbull, A. S. Davies, T. J. Kessler, D. Haberberger, J. P. Palastro, S.-W. Bahk, I. A. Begishev, R. Boni, S. Bucht, J. Katz, and J. L. Shaw. Spatiotemporal control of laser intensity. *Nature Photonics*, 12:262–265, 2018.
- [25] H. E. Kondakci and A. F. Abouraddy. Diffraction-free pulsed optical beams via space-time correlations. *Optics Express*, 24(25):28659–28668, 2016.
- [26] H. E. Kondakci and A. F. Abouraddy. Diffraction-free space-time light sheets. *Nature Photonics*, 11:733–740, 2017.
- [27] B. Bhaduri, M. Yessenov, and A. F. Abouraddy. Meters-long propagation of diffraction-free space-time light-sheets. *Optics Express*, 26(16):20111–20121, 2018.
- [28] B. Bhaduri, M. Yessenov, D. Reyes, J. Pena, M. Meem, S. R. Fairchild, R. Menon, M. Richardson, and A. F. Abouraddy. Broadband space-time wave packets propagating 70 m. *Optics Letters*, 44(8):2073–2076, 2019.
- [29] J. P. Palastro, D. Turnbull, S.-W. Bahk, R. K. Follett, J. L. Shaw, D. Haberberger, J. Bromage, and D. H. Froula. Ionization waves of arbitrary velocity driven by a flying focus. *Physical Review A*, 97:033835, 2018.
- [30] S. W. Jolly, O. Gobert, A. Jeandet, and F. Quéré. Controlling the velocity of a femtosecond laser pulse using refractive lenses. *Optics Express*, 28(4):4888–4897, 2020.
- [31] D. Turnbull, P. Franke, J. Katz, J. P. Palastro, I. A. Begishev, R. Boni, J. Bromage, A. L. Milder, J. L. Shaw, and D. H. Froula. Ionization waves of arbitrary velocity. *Physical Review Letters*, 120(22):225001, 2018.
- [32] P. Franke, D. Turnbull, J. Katz, J. P. Palastro, I. A. Begishev, J. Bromage, J. L. Shaw, R. Boni, and Dustin H. Froula. Measurement and control of large diameter ionization waves of arbitrary velocity. *Optics Express*, 27(22):31978–31988, 2019.
- [33] D. Turnbull, S. Bucht, A. Davies, D. Haberberger, T. Kessler, J. L. Shaw, and D. H. Froula. Raman amplification with a flying focus. *Physical Review Letters*, 120:024801, 2018.
- [34] A. J. Howard, D. Turnbull, A. S. Davies, P. Franke, D. H. Froula, and J. P. Palastro. Photon acceleration in a flying focus. *Physical Review Letters*, 123:124801, 2019.
- [35] D. Ramsey, P. Franke, T. T. Simpson, D. H. Froula, and J. P. Palastro. Vacuum acceleration of electrons in a dynamic laser pulse. *Physical Review E*, 102:043207, 2020.
- [36] H. E. Kondakci and A. F. Abouraddy. Optical space-time wave packets having arbitrary group velocities in free space. *Nature Communications*, 10:929, 2019.
- [37] B. Bhaduri, M. Yessenov, and A. F. Abouraddy. Space-time wave packets that travel in optical materials at the speed of light in vacuum. *Optica*, 6(2):139–146, 2019.
- [38] M. Yessenov and A. F. Abouraddy. Accelerating and decelerating space-time optical wave packets in free space. *Physical Review Letters*, 125:233901, 2020.
- [39] Z. Li and J. Kawanaka. Optical wave-packet with nearly-programmable group velocities. *Communications Physics*, 3:211, 2020.
- [40] F. Quéré, H. Vincenti, A. Borot, S. Monchocé, T. J. Hammond, K. T. Kim, J. A. Wheeler, C. Zhang, T. Ruchon, T. Augustine, J. F. Hergott, D. M. Villeneuve, P. B. Corkum, and R. Lopez-Martens. Applications of ultrafast wavefront rotation in highly nonlinear optics. *Journal of Physics B: Atomic, Molecular and Optical Physics*, 47:124004, 2014.
- [41] H. Vincenti and F. Quéré. Attosecond lighthouses: How to use spatiotemporally coupled light fields to generate isolated attosecond pulses. *Physical Review Letters*, 108:113904, 2012.
- [42] J. A. Wheeler, A. Borot, S. Monchoce, H. Vincenti, A. Ricci, A. Malvache, R. Lopez-Martens, and F. Quéré. Attosecond lighthouses from plasma mirrors. *Nature Photonics*, 6:829–833, 2012.
- [43] K. T. Kim, C. Zhang, T. Ruchon, J.-F. Hergott, T. Augustine, D. M. Villeneuve, P. B. Corkum, and F. Quéré. Photonic streaking of attosecond pulse trains. *Nature Photonics*, 7:651–656, 2013.
- [44] T. Augustine, O. Gobert, T. Ruchon, and F. Quéré. Attosecond lighthouses in gases: A theoretical and numerical study. *Physical Review A*, 93:033825, 2016.
- [45] S. Akturk, X. Gu, E. Zeek, and R. Trebino. Pulse-front tilt caused by spatial and temporal chirp. *Optics Express*, 12(19):4399–4410, 2004.
- [46] I. P. Christov. Propagation of femtosecond light pulses. *Optics Communications*, 53(6):364–366, 1985.
- [47] R. W. Ziolkowski and J. B. Judkins. Propagation characteristics of ultrawide-bandwidth pulsed gaussian beams. *Journal of the Optical Society of America A*, 9(11):2021–2030, 1992.
- [48] S. Feng, H. G. Winful, and R. W. Hellwarth. Gouy shift and temporal reshaping of focused single-cycle electromagnetic pulses. *Optics Letters*, 23(5):385–387, 1998.
- [49] M. A. Porras. Diffraction effects in few-cycle optical pulses. *Physical Review E*, 65:026606, 2002.
- [50] M. A. Porras. Characterization of the electric field of focused pulsed gaussian beams for phase-sensitive interactions with matter. *Optics Letters*, 34(10):1546–1548, 2009.
- [51] M. A. Porras. Carrier-envelope phase shift of few-cycle pulses along the focus of lenses and mirrors beyond the nonreshaping pulse approximation: the effect of pulse chirp. *Journal of the Optical Society of America B*, 29(12):3271–3276, 2012.
- [52] D. Hoff, M. Krüger, L. Maisenbacher, A. M. Saylor, G. G. Paulus, and P. Hommelhoff. Tracing the phase of focused broadband laser pulses. *Nature Physics*, 13:947–952, 2017.
- [53] M. A. Porras, Z. L. Horváth, and B. Major. Three-dimensional carrier-envelope-phase map of focused few-cycle pulsed gaussian beams. *Physical Review A*, 98:063819, 2018.
- [54] D. Hoff, M. Krüger, L. Maisenbacher, G. G. Paulus, P. Hommelhoff, and A. M. Saylor. Using the focal phase to control attosecond processes. *Journal of Optics*, 19:124007, 2017.
- [55] Y. Zhang, D. Zille, D. Hoff, P. Wustelt, D. Würzler, M. Möller, A. M. Saylor, and G. G. Paulus. Observing the importance of the phase-volume effect for few-cycle light-matter interactions. *Physical review Letters*, 124:133202, 2020.
- [56] C. F. R. Caron and R. M. Potvliege. Free-space propagation of ultrashort pulses: Space-time couplings in gaussian pulse beams. *Journal of Modern Optics*, 46(13):1881–1891, 1999.
- [57] L. J. Wong and I. Kaminer. Ultrashort tilted-pulse-front pulses and nonparaxial tilted-phase-front beams. *ACS*

- Photonics*, 4:2257–2264, 2017.
- [58] R. W. Ziolkowski. Localized transmission of electromagnetic energy. *Physical Review A*, 39(4):2005–2033, 1989.
- [59] R. W. Hellwarth and P. Nouchi. Focused one-cycle electromagnetic pulses. *Physical Review E*, 54(1):889–895, 1996.
- [60] A. Zdagkas, N. Papasimakis, V. Savinov, and N. I. Zheludev. Space-time nonseparable pulses: Constructing isodiffracting donut pulses from plane waves and single-cycle pulses. *Physical Review A*, 102:063512, 2020.
- [61] V. Bagini, R. Borghi, F. Gori, A. M. Pacileo, M. Santarsiero, D. Ambrosini, and G. Schirripa Spagnolo. Propagation of axially symmetric flattened gaussian beams. *Journal of the Optical Society of America A*, 13(7):1385–1394, 1996.
- [62] E. Wolf. Electromagnetic diffraction in optical systems I. an integral representation of the image field. *Proceedings of the Royal Society A*, 253:349–357, 1959.
- [63] B. Richards and E. Wolf. Electromagnetic diffraction in optical systems II. structure of the image field in an aplanatic system. *Proceedings of the Royal Society A*, 253:358–379, 1959.
- [64] S. Pelchat-Voyer and M. Piché. Clarifications on the gouy phase of radially polarized laser beams. *Journal of the Optical Society of America A*, 37(9):1496–1504, 2020.
- [65] S. W. Jolly, O. Gobert, and F. Quéré. Spatio-temporal characterization of ultrashort laser beams: a tutorial. *Journal of Optics*, 22(10):103501, 2020.
- [66] B. Alonso, I. Lopez-Quintas, W. Holgado, R. Drevinskas, P. G. Kazansky, C. Hernández-García, and Í. J. Sola. Complete spatiotemporal and polarization characterization of ultrafast vector beams. *Communication Physics*, 3:151, 2020.
- [67] Spencer W. Jolly. RPLB-STC. <https://github.com/spencerjolly/RPLB-STC>.